MODELING THE INFLUENCE OF STITCHING ON DELAMINATION GROWTH IN STITCHED WARP-KNIT COMPOSITE LAP JOINTS

E.H. Glaessgen[1], I.S. Raju[2] and C.C. Poe, Jr.[2]

[1]National Research Council
[2]Mechanics of Materials Branch
NASA Langley Research Center, Hampton, VA, 23681

SUMMARY: The effect of stitches on the failure of a single lap joint configuration was determined in a combined experimental and analytical study. The experimental study was conducted to determine debond growth under static monotonic loading. The stitches were shown to delay the initiation of the debond and provide load transfer beyond the load necessary to completely debond the stitched lap joint. The strain energy release rates at the debond front were calculated using a finite element-based technique. Models of the unstitched configuration showed significant values of modes I and II across the width of the joint and showed that mode III is zero at the centerline but increases near the free edge. Models of the stitched configuration showed that the stitches effectively reduced mode I to zero, but had less of an effect on modes II and III.

KEYWORDS: virtual crack closure technique, plate finite elements, textile composites, stitching, debonding, lap joints

INTRODUCTION

Structures manufactured from stitched warp-knit textile composite materials offer advantages in manufacturability and damage tolerance over conventional composite and metallic structures.[1] However, it is often impossible to manufacture a complete component as an integral unit, and hence separate sections of the component need to be joined together. Rather than bolting or bonding sections, stitching is used in the textile composites discussed here. Improvements in damage tolerance are observed because the Kevlar stitches tend to prevent propagation of debonds and delaminations that may be caused by in-plane and out-of-plane loadings.[2]

The objective of this paper is to quantify the effect of stitches on the response of lap joints in warp knit carbon epoxy textile composites under monotonic tensile loading. Failure mechanisms and failure loads of unstitched and stitched lap joints are determined using a combined analytical and experimental technique. Comparisons are made between the experimentally determined failure loads of the stitched and similar unstitched lap joint panels to assess the contribution of the stitches to preventing delamination growth. Strain energy release rates and stitch forces are evaluated using finite element analyses.

LAP JOINT CONFIGURATION

A stitched lap joint subjected to remote tensile loading is shown in Figure 1. The configurational parameters of the joint considered in this study are the length of the composite, L_1, the length of the overlap, L_2, the width of the coupon, b, and the thickness of the material, t and are shown in Figure 2. Material and skin thicknesses that are representative of the hybrid IM7/3501-6 and AS4/3501-6 warp-knit fabric stitched composite upper wing skin are considered.[1] The material consists of IM7 yarns in the axial direction and AS4 yarns in the off-axis directions. Each stack of material is assumed to be oriented with its primary axis in the x-direction and having a thickness of 0.140 cm. The equivalent laminate stacking sequence of each stack of material is $(45/-45/0/90/0/-45/45)_{ns}$ where n=2 for both of the joined laminates.

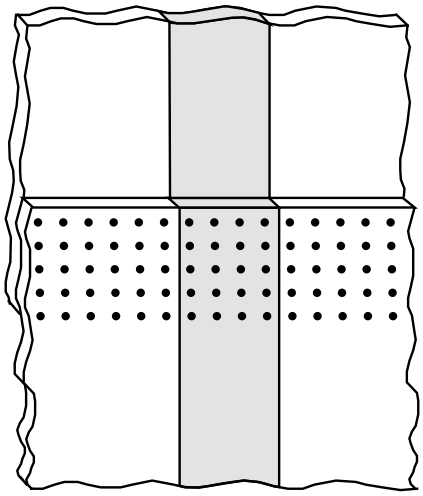

Figure 1. Stitched lap joint configuration.

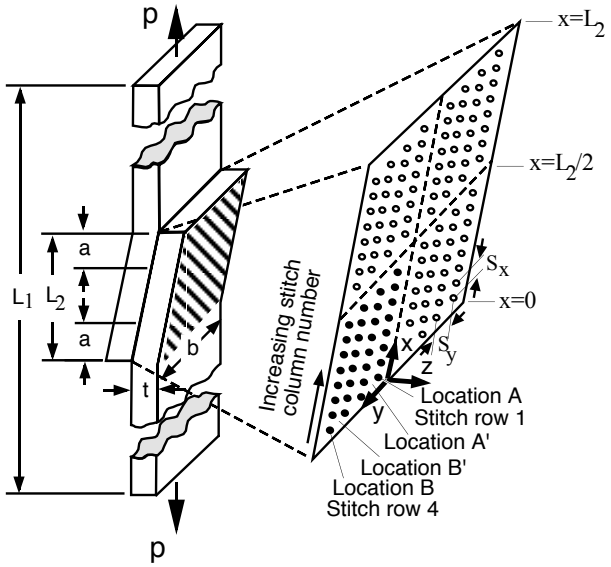

Figure 2. Stitched joint configuration (S_x=S_y=0.318 cm., t=0.279 cm., b=2.54 cm., L_1=68.6 cm., L_2=9.37 cm.).

Unstitched and stitched lap joint specimens were fabricated with dimensions presented in Figure 2. The specimens were loaded in monotonic tension at a rate of 0.127 cm./min. Debonds initiated and grew at the ends of the lap joints. Increase in debond length with increasing load was determined using x-ray radiographs.

FINITE ELEMENT ANALYSIS

Three-dimensional modeling and analysis of the complex lap joint configuration shown in Figure 1 may require a large finite element model with several thousand degrees of freedom.

However, considerable insight into the behavior of such a complicated configuration can be obtained by studying a much simpler configuration such as the strip lap joint configuration shown in Figure 2 while reducing modeling complexity.

The method of analysis uses plate elements to model the configuration, nonlinear fastener elements to model the stitches, and multipoint constraints to model the contact problem. The specimen configurational parameters are shown in Figure 2. Debond lengths, a, in the range 0.635 cm. to 3.81 cm. are considered.

A finite element model of the test specimens was developed. Two cases of transverse (y-direction) boundary conditions were considered and simulate both the finite width lap joint that was tested in the experimental program and an infinite width lap joint similar to the structure shown in Figure 1. The finite width lap joint configuration is modeled to provide insight into the experimental results while the infinite width lap joint configuration is modeled to eliminate the effect of free edge boundary conditions on strain energy release rates and stitch forces in the lap joint configuration of Figure 1. Thus, results from the finite width and infinite width configurations should bound the response of actual stitched lap joint configurations. Analyses for both the finite and infinite width configurations use experimentally determined load vs. crack length curves that were developed from an experimental study of unstitched and stitched lap joints in the configuration shown in Figure 2.[3] The analyses were performed in increments of debond length, a, of 0.318 cm.

Material Properties

In these analyses, the laminates are assumed to be homogeneous with axial properties determined experimentally and all others estimated using the equivalent stacking sequence and classical lamination theory as

E_{11}=80.7 *GPa*	μ_{12}=17.2 *GPa*	υ_{12}=0.40
E_{22}=35.4 *GPa*	μ_{13}=12.2 *GPa*	υ_{13}=0.30
E_{33}=12.3 *GPa*	μ_{23}=6.07 *GPa*	υ_{23}=0.30

where E_{ii}, μ_{ij}, υ_{ij} (i,j=1,2,3) are the Young's moduli, shear moduli, and Poisson's ratio, respectively, and the subscripts 1,2,3 represent the fiber, transverse and out-of-plane directions, respectively.

Strain Energy Release Rates

The lap joint configuration was modeled with the STAGS (Structural Analysis of General Shells) finite element code using a 9-node quadratic shear deformable plate/shell element.[4] The virtual crack closure technique (VCCT)[5,6] was used to calculate strain energy release rates, G, with plate elements using the techniques discussed in references 7-9. A comparison of strain energy release rates computed with the plate element-based models and similar plane strain element-based models for skin-stiffener configurations without stitching is discussed in

reference 9. Additional considerations that arise from debond modeling with plate elements are discussed in reference 8.

Modeling Stitches

The configurations were analyzed with a geometrically nonlinear finite element analysis within the STAGS finite element code. The plate element-based modeling technique does not allow through-the-thickness modeling of details such as the stitches; nor does it allow nodal connections other than at the plate element reference surface. Thus, the stitches are modeled as STAGS fastener elements.

The fastener elements are imposed as nonlinear springs offset by rigid links within the plate element model.[4] Fastener elements representing the stitches have both axial and shear stiffnesses, K_{axial} and K_{shear} as determined in reference 10. Failure of the stitches occurs at a load of 258 N per stitch in tension and 169 N per stitch in shear.[10] Only the stitches behind the debond front are considered since the upper and lower plate elements ahead of the debond front are coupled using constraint equations to have identical translational displacements. The fastener element location spacing presented in Figure 2 coincides with plate element nodal locations.

Modeling the Contact Problem

In the finite element analysis, contact of the debonded faces is allowed, while interpenetration is not. The contact problem was modeled using multipoint constraints rather than gap elements because the no-penetration condition could be imposed exactly with the multipoint constraints whereas the STAGS gap elements enforce no-penetration to a small but finite tolerance that is significant in this analysis.

EXPERIMENTAL RESULTS

Since a limited amount of the material was available, only two replicates of each specimen configuration were tested. The failure loads of these specimens are presented in Table 1. The unstitched lap joint specimens catastrophically failed at the interface. The stitched lap joint specimens completely debonded at the interface while maintaining their load carrying capability. Final failure of these specimens was due to combined tensile and bending loads at the ends of the lap joint. Thus, the failure loads listed for the stitched specimen represent lower bounds.

Radiographic images were taken at periodic intervals during loading to determine the length of the debond at each applied load level. Figures 3(a) and 3(b) present the damage within representative lap joints of the unstitched and stitched configurations, respectively. For convenience in presentation, the line corresponding to $x=L_2$ in Figure 2 is denoted as the top of the lap joint, while the line corresponding to $x=0$ is denoted as the bottom of the lap joint.

Table 1: Test Specimen Failure Loads

Specimen	Unstitched (U) or Stitched (S)	Failure Load, kN
Slap 1-1	U	20.65
Slap 1-2	U	19.61
Slap 1-1S	S	52.60
Slap 1-2S	S	51.73

Figures 3(a) and 3(b) present the damage at loads near the failure loads within representative lap joints of the unstitched and stitched configurations, respectively. Figure 3(a) shows the unstitched lap joint of length L_2=9.37 cm. with a debond of length, a, growing from the top of the lap at a load of 19.1 kN. No debonds were observed growing near the bottom of the lap. This could be the result of a small asymmetry in the specimen or load frame and is likely due to the debond at the top of the lap initiating first and relieving the driving force at the bottom of the lap. The primary debond shown in Figure 3(a) grew at the interface of ±45° yarns. A split initiated in the 45° yarns and allowed a secondary debond to initiate and grow between the 45° and 0° yarns as shown in Figure 3(a). Catastrophic failure due to unstable debond growth was observed at 20.7 kN.

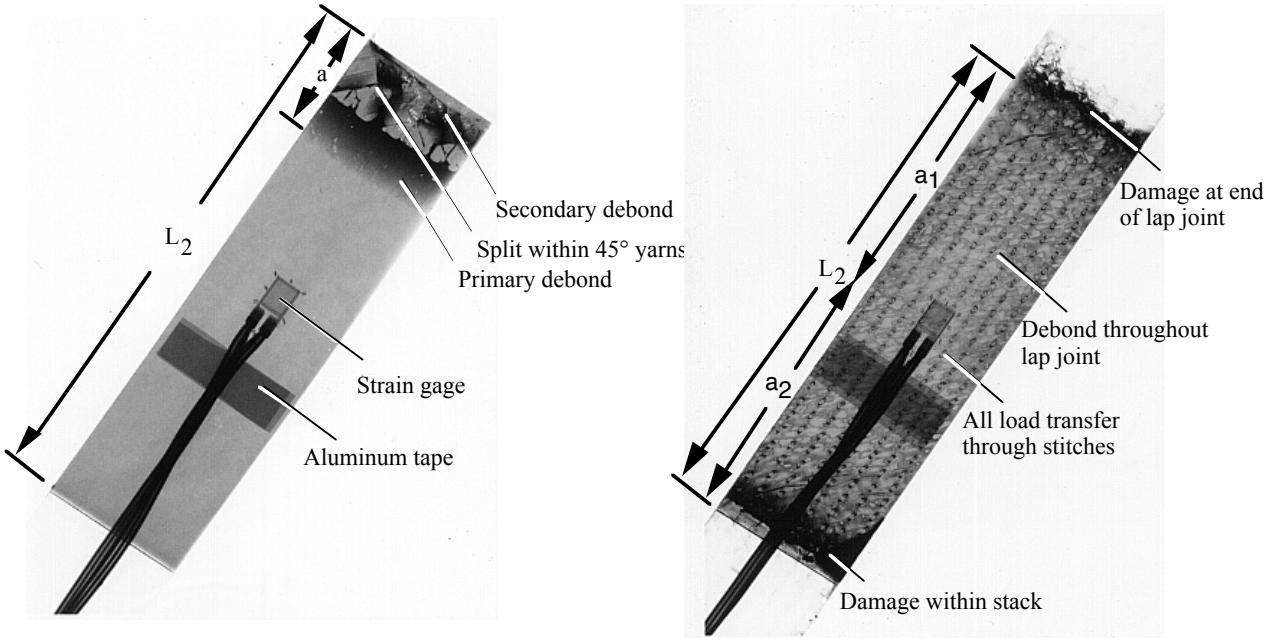

(a) Unstitched specimen at P=19.14 kN (a=1.98 cm.). (b) Stitched specimen at P=49.12 kN(a_1=4.68 cm., a_2=4.68 cm.).

Figure 3. Radiographs showing debond in lap joint.

Figure 3(b) shows a completely debonded stitched lap joint that maintained a load of 49.1 kN. Debonds initiated and grew from both ends of the joint completely debonding the lap joint. Final failure occurred at 52.6 kN and was not due to stitch failure but was due to a tensile and bending stress failure at the ends of the lap. The value of 52.6 kN may then be treated as a lower bound of load carrying capability for this specimen. The average failure load of the stitched lap joints was 2.6 times the failure load of the unstitched lap joints.

ANALYTICAL RESULTS

Experimentally determined average debond length vs. load curves for the unstitched and stitched single lap joints are given in reference 3 and are used as input parameters in the analysis. In general, the lap joint configurations may exhibit mode I, mode II and mode III strain energy release rates. Also, although a straight debond front is employed to simplify the analyses, a variation in both strain energy release rate and stitch force may exist along the length (x-) and across the width (y-) of the finite width lap joint. In the results that follow, quantities for the finite width configurations are given at y-direction locations corresponding to: an interior row of stitches near the centerline of the stitched configuration (stitch row 1); an exterior row of stitches near the edge of the stitched configuration (stitch row 4); and intermediate locations between stitch rows 1 and 2 and stitch rows 3 and 4. These later locations are considered only for the stitched configuration. The y locations denoted as locations A, B, A' and B' are located at y=0.159 cm., y=1.11 cm., y=0.318 cm. and y=0.953 cm., respectively, from the configuration centerline. Quantities for both the unstitched and stitched infinite width configurations are also provided. When cylindrical bending repeating unit boundary conditions (v=0, θ_x=0 on y=0, $b/2$ in Figure 2) are applied to the models, the calculated G-values are constant in the y-direction for the unstitched configuration and periodic in the y-direction for the stitched configuration.

Figures 4 through 6 show the individual modes of the strain energy release rates, the y-direction distribution of strain energy release rates, and the stitch forces, respectively, as functions of debond length. The values of strain energy release rate for loads corresponding to the debond lengths in Figure 4 are significantly greater than the G_{Ic} and G_{IIc} values determined for typical carbon / brittle epoxy material systems.[11] In reference 11, G_{Ic} and G_{IIc} for AS4/3501-6 composites are given as 0.08 kJ/m^2 and 0.55 kJ/m^2, respectively. Both the unstitched and stitched lap joint configurations are able to sustain these high G-values due to several energy absorbing phenomena. In the unstitched material, splitting of the 45° yarns and the formation and growth of a secondary debond between the 45° and 0° yarns seen in Figure 3(a) contribute to the apparent high value of fracture toughness. In the stitched material, there is also some damage within the stacks of material as shown in Figure 3(b). This occurs over only a small portion of the debonded length of the stitched lap joint. A full three-dimensional analysis may be required to account for the individual contributions of each of the damage mechanisms. However, using the debond length and applied load from the experiment, the plate element-based analyses can predict the effective values of G as seen in Figures 4 and 5. These G-values can then be used as ranking parameters. Note that the loads considered for the stitched configuration are much greater than the loads considered for the unstitched configuration as shown in Table 1, so Figures 4(a) and 4(b) cannot be compared directly.

Figure 4(a) shows G-values plotted against debond length for the unstitched configuration with a debond at only one end of the single lap joint corresponding to the radiograph shown in Figure 3(a). Figure 4(a) shows two nonzero components of G near the centerline of the finite width lap joint (Location A) and three nonzero components of G near the free edge of the finite width lap joint (Location B). Mode I increases at both locations as the debond

grows. Mode II is the largest component of energy release rate and also increases with increasing debond length. Mode III has a value near zero (thus, not shown) in the interior at location *A* but increases near the free edge (Location *B*). Values of $2a/L_2$ greater than 0.51 correspond to catastrophic debond growth in the unstitched configuration shown in Figure 3(a).

The energy release rates computed at locations *A* and *B* in the finite width configuration bound the energy release rates computed for the infinite width configuration (shown as G_I^∞ and G_{II}^∞ in Figure 4(a). This is a result of the cylindrical bending boundary conditions in the infinite width models preventing anticlastic deformation while the stress free boundary conditions in the finite width models do not. Additionally, the cylindrical bending boundary conditions in the infinite width models require mode III to be identically zero.

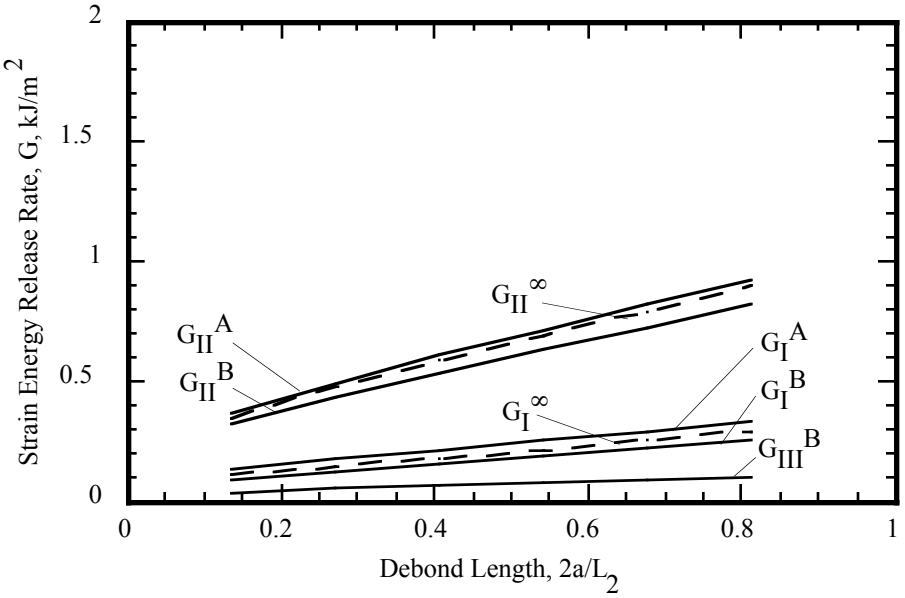

Figure 4(a). Strain energy release rate in unstitched lap joint.

Figures 4(b) and 5 show the *G*-values plotted as functions of debond length and lap joint width, respectively, for the stitched configuration with a debond at each end of the single lap joint corresponding to the radiograph shown in Figure 3(b). The computed values of *G* in Figure 4(b) are at discrete locations between the stitch columns and a smooth curve is drawn between the points. Figure 4(b) shows one nonzero component of *G* at locations *A* and *A'* and two nonzero components of *G* at locations *B* and *B'*. For all debond lengths at all locations, the mode I component is near zero. As with the unstitched configuration, mode II is the dominant component and is seen to increase with debond length. Although G_{II} increases with increasing debond length, the stitches prevent the debond growth from becoming unstable. As seen in Figure 5, mode II is significantly larger at the locations between the stitches (Locations *A'* and *B'*) than at the stitch locations (Locations *A* and *B*) indicating some localization of the effectiveness of the stitches. As in the unstitched configuration, mode III has a value near zero in the interior (Locations *A* and *A'*) but increases near the edge (Locations *B* and *B'*).

Cylindrical bending boundary conditions also prevent anticlastic deformation in the infinitely wide stitched lap joint. The resulting G_{II}^∞ is periodic across the width of the joint as shown

in Figure 5. For long debonds ($2a/L_2$)=0.813, the largest values of mode II are found at ($2y/b$)=0 for the infinite width configuration and ($2y/b$)=0.969 for the finite width configuration. Because of the cylindrical bending boundary conditions mode III is identically zero at y=0, b/2 and nearly zero for other values of y in this range.

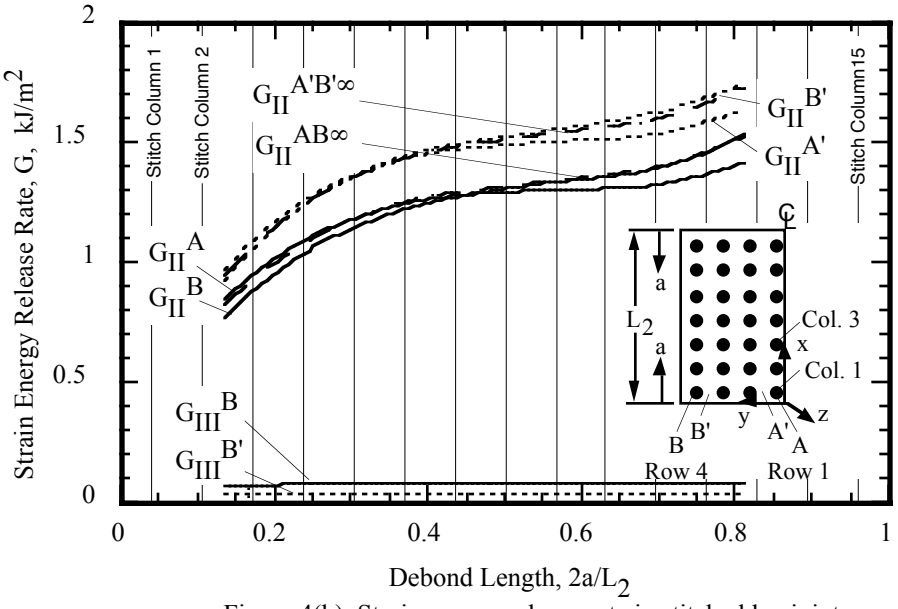

Figure 4(b). Strain energy release rate in stitched lap joint.

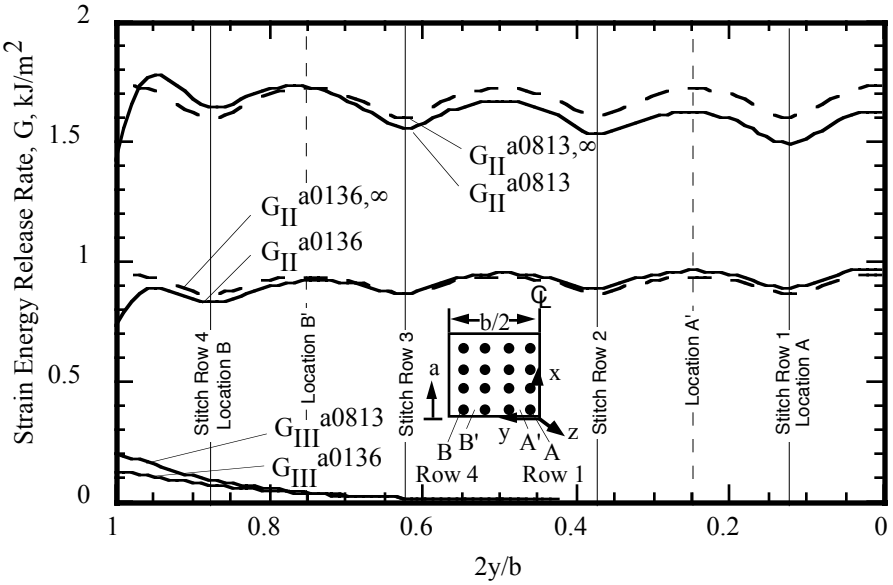

Figure 5. Strain energy release rate distribution for $2a/L_2$=0.136 and 0.813.

The dominant component of stitch force is longitudinal shear and is presented in Figure 6. The figure shows how each of the stitches begins to carry load as the debond of length, a, passes its location in the model. Since the results were evaluated from the finite element model with increments of debond length of 0.318 cm. ($2a/L_2$)=0.0678, the force in the stitches for debond lengths corresponding to the interval between the stitch location and the next whole increment of debond length is not known and is represented by the thin lines.

Figures 6(a) and 6(b) show the longitudinal shear forces (F_{xz}) in stitch rows 1 and 4, respectively. In both rows, all stitches are loaded and show increasing values of shear force as the debond grows. The values shown in Figures 6(a) and 6(b) for stitch rows 1 and 4 are almost identical. This is not unexpected as G_{II} values at locations *A* and *B* are similar. The load sharing among all of the stitches is a result of the stitch nonlinearity and contributes to the increase in strength of the stitched lap joints that were tested in the experimental study. The longitudinal shear stitch forces for stitches in the infinitely wide lap joint do not vary with *y* location and are represented by the dashed lines in Figure 6.

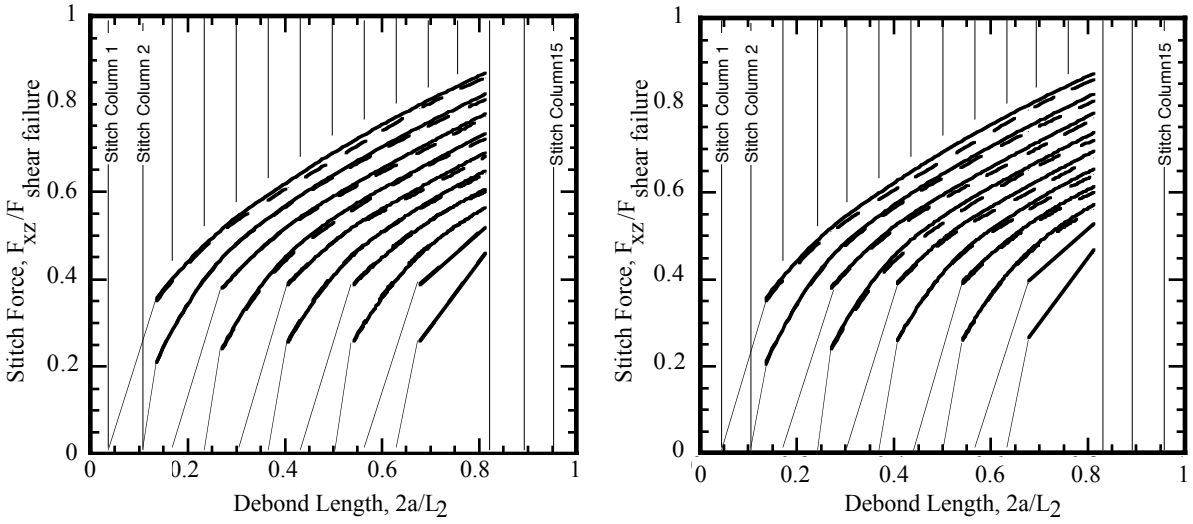

(a) Longitudinal shear forces in stitch row 1.

(b) Longitudinal shear forces in stitch row 4.

Figure 6. Stitch forces.

CONCLUDING REMARKS

The effect of stitches on the failure of finite width and infinite width single lap joint configurations was studied. An experimental program was conducted to determine the loads necessary to grow the debond through complete debonding of the specimens. Modeling was performed using a method that uses the virtual crack closure technique to calculate the strain energy release rates, plate elements to model the configuration, nonlinear fastener elements to model the stitches and multipoint constraints to model the contact problem.

The stitches were shown to delay the initiation of the debond and provide load transfer beyond the load necessary to completely debond the lap joint. For the configurations considered, the failure load of the stitched lap joints was about two and a half times the failure load of the unstitched lap joints.

Models of the finite width unstitched configuration showed that the nonzero components of strain energy release rate vary nearly linearly with debond length. All three modes increase with increasing debond length at locations near the configuration centerline and near the configuration free edge. Mode II is the largest of the three components, while mode III is the smallest. An infinite width lap joint was modeled by applying cylindrical bending repeating unit boundary conditions to the edges of the model. Values of modes I and II were bounded

by the values of the corresponding modes of the finite width lap joint and mode III was identically zero.

Models of the finite width stitched configuration showed that one nonzero component of G exists near the centerline while two nonzero components exist near the free edge. The stitches reduce G_I to near zero values for all debond lengths. However, the stitches are much less effective in reducing G_{II} as it is the dominant component and is seen to increase over the entire range of debond lengths considered. The effectiveness of the stitches in reducing mode II is further reduced at locations between the rows of stitching. Mode III is significant only near the free edge. Values of mode II for an infinitely wide lap joint are periodic and of about the same magnitude as those for a finite width lap joint. Mode III is nearly zero. Longitudinal shear force is transferred by all rows of stitches in the debonded region and increases with increasing debond length.

REFERENCES

1. Dow, M.B. and Dexter, H.B., "Development of Stitched, Braided and Woven Composite Structures in the ACT Program and at Langley Research Center," *NASA TP-97-206234*, November 1997.
2. Wang, J.T., Jegley, D.C., Bush, H.G. and Hinrichs, S.C., "Correlation of Structural Analysis and Test Results for the McDonnell Douglas Stitched/RFI All-Composite Wing Stub Box," *NASA TM-110267*, 1996.
3. Glaessgen, E.H., Raju, I.S. and Poe, C.C., "Delamination and Stitch Failure in Stitched Composite Joints," *40th AIAA/ASME/ASCE/AHS Structures, Structural Dynamics and Materials Conference*, AIAA Paper 99-1247, 1999.
4. Brogan, F.A., Rankin, C.C., Cabiness, H.D. and Loden, W.A., *STAGS User Manual*, Lockheed Martin Missiles and Space Co., July 1996.
5. Rybicki, E.F. and Kanninen, M.F., "A Finite Element Calculation of Stress Intensity Factors by a Modified Crack Closure Integral," *Engineering Fracture Mechanics*, Vol. 9, 1977, pp. 931-938.
6. Raju, I.S., "Calculation of Strain-Energy Release Rates with Higher Order and Singular Finite Elements," *Engineering Fracture Mechanics*, Vol. 28, No. 3, 1987, pp. 251-274.
7. Wang, J.T. and Raju, I.S., "Strain Energy Release Rate Formulae for Skin-Stiffener Debond Modeled with Plate Elements," *Engineering Fracture Mechanics*, Vol. 54, No. 2, 1996, pp. 211-228.
8. Glaessgen, E.H., Riddell, W.T. and Raju, I.S., "Effect of Shear Deformation and Continuity on Delamination Strain Energy Release Rate," *39th AIAA/ASME/ASCE/AHS Structures, Structural Dynamics and Materials Conference*, AIAA Paper 98-2023-CP, 1998.
9. Glaessgen, E.H., Raju, I.S. and Poe, Jr., C.C., "Plate Element-Based Models for Mixed-Mode Debonding of Stitched Stiffened Panels," *STP 1360, Fatigue and Fracture Mechanics: 30th Volume*, ASTM, 1998, in press.
10. Adams, D.O., "Stitch Compliance in Delaminated Composites," *29th SAMPE Technical Conference*, Orlando, FL, October 28-31, 1997.
11. Reeder, J.R., "A Bilinear Failure Criterion for Mixed-Mode Delamination," *ASTM STP 1206*, E.T. Camponeschi, Jr., Ed., ASTM, Philadelphia, PA, 1993, pp. 303-322.